

Article

Electron Beam-Melting and Laser Powder Bed Fusion of Ti6Al4V: Transferability of Process Parameters

Sandra Megahed *, Vadim Aniko and Johannes Henrich Schleifenbaum

Digital Additive Production (DAP), RWTH Aachen University, Campus-Boulevard 73, 52074 Aachen, Germany
* Correspondence: sandra@megahed.de

Abstract: Metal powder bed-based Additive Manufacturing (AM) technologies, such as Electron Beam-Melting (EBM) and Laser Powder Bed Fusion (LPBF), are established in several industries due to the large design freedom and mechanical properties. While EBM and LPBF have similar operating steps, process-specific characteristics influence the component design. The differences in the energy coupling lead to differing solidification conditions, microstructures, and, thus, mechanical properties. The surface finish and geometrical accuracy are also affected. As opposed to LPBF, EBM powder layers are preheated prior to selective melting. In this study, similar volume energy densities in LPBF and EBM were used to manufacture Ti6Al4V test geometries to assess the process transferability. Since the energy coupling of LPBF and EBM differ, heat source absorption was considered when calculating the volume energy density. Even when a similar volume energy density was used, significant differences in the component quality were found in this study due to specific respective process constraints. The extent of these constraints was investigated on voluminous samples and support-free overhanging structures. Overhang angles up to 90° were manufactured with LPBF and EBM, and characterized with regard to the relative density, surface roughness, and geometric compliance.

Keywords: Electron Beam-Melting; EBM; Laser Powder Bed Fusion; LPBF; Ti6Al4V; volume energy density; absorption; support-free overhang; hardness; surface roughness



Citation: Megahed, S.; Aniko, V.; Schleifenbaum, J.H. Electron Beam-Melting and Laser Powder Bed Fusion of Ti6Al4V: Transferability of Process Parameters. *Metals* **2022**, *12*, 1332. <https://doi.org/10.3390/met12081332>

Academic Editors: Vera Popovich and Thorsten Becker

Received: 10 July 2022

Accepted: 5 August 2022

Published: 9 August 2022

Publisher's Note: MDPI stays neutral with regard to jurisdictional claims in published maps and institutional affiliations.



Copyright: © 2022 by the authors. Licensee MDPI, Basel, Switzerland. This article is an open access article distributed under the terms and conditions of the Creative Commons Attribution (CC BY) license (<https://creativecommons.org/licenses/by/4.0/>).

1. Introduction

Metal powder bed fusion is a manufacturing process in which a beam energy source selectively melts powder layer-by-layer based on a 3D Computer-Aided Design (CAD) model [1–4]. Due to the difference in heat source, it is often assumed that LPBF and EBM operate with differing volume energy densities. Contrary to LPBF, during EBM, each powder layer is preheated and sintered using a defocused beam. Once the build is complete, loose powder is brushed off of the LPBF component. EBM components require more rigorous de-powdering processes to remove the sintered powder. If necessary, the built components undergo further postprocessing (e.g., sand blasting, heat treatment, hot isostatic pressing, etc.) [2].

1.1. Laser Powder Bed Fusion (LPBF)

Most LPBF machines can heat a build platform up to 200 °C in order to reduce temperature gradients [5]. The process chamber is filled with inert gas, which flows over the powder bed (remaining O₂ content up to ~ 500 ppm) [6,7]. The absorption of a metal is temperature-dependent and rises with increasing temperature [8,9]. Other factors affecting laser absorption include melting conditions, defects, and oxide films [8].

The typical powder size distribution (PSD) for LPBF lies in the range of 10–63 µm. In order to reuse powder, it must be sieved [10,11]. Sieving removes spatter and large powder particles that would affect the required energy density to homogeneously melt the powder. The as built surface roughness ranges from 5 to 40 µm depending on the process parameters and build orientation [12]. A typical surface roughness of vertical walls is Ra = 11 µm [13].

During LPBF, materials solidify at high cooling rates of about 10^6 K/s, resulting in a very fine microstructure [14]. According to the Hall-Petch relation, a fine microstructure leads to high material hardness [15]. Ti6Al4V is an $\alpha + \beta$ alloy. Due to rapid cooling during the LPBF process, metastable α' martensite with prior β -texturization in the build direction is formed [16]. The metastable α' martensite is characterized by high strength at the expense of low ductility [17]. LPBF samples show an ultimate tensile strength and yield a stress of approximately 1200 MPa and 1100 MPa respectively [17–19]. Ti6Al4V manufactured with laser AM technologies achieves an elongation between 4% and 19% [17,18].

1.2. Electron Beam-Melting (EBM)

The EBM process runs under a vacuum at an absolute pressure of $\sim 50 \times 10^{-4}$ mbar (i.e., 0.5 Pa) [13]. The electron beam also necessitates the powder to be sintered or otherwise electrostatic forces lead to clouds of charged particles (i.e., arc trips) in the build chamber [20]. Powder layers can be preheated and sintered up to 1100 °C by using a defocused electron beam [13]. As a result, temperature gradients between the melt pool and powder bed are lowered and thermal stresses are significantly reduced. Process parameters affect the dimensional quality of the EBM parts [21].

The recommended PSD for EBM is 45–105 μm [13]. Smaller powder sizes cannot be used since that would lead to process instabilities [13]. However, studies have been carried out with a powder size similar to that in LPBF to reduce surface roughness [22]. Larger powder sizes do not pose an issue [13]. Powder can be recycled up to 12 times [23].

A vertical surface roughness (R_a) of approximately 30 μm is reported by [24] using a layer thickness of 70 μm . A surface roughness (R_a) between 6 and 19 μm can be achieved by reducing the layer thickness to 50 μm [25]. EBM processes conduct an in situ heat treatment of the part due to the preheating and the elevated temperature of the build chamber [13]. The microstructure is therefore larger compared to the microstructure of LPBF. In the case of Ti6Al4V, the columnar β -structure is replaced by α lamellas and a small amount of the β phase. The resulting ultimate tensile strength is approximately 1050–1200 MPa. The yield stress is around 900–1100 MPa and ductilities of up to 17% are achieved [16,26,27].

Several comparisons of the LPBF and EBM processes with a focus on the microstructure have been conducted [17,28–32]. The process-parameter transferability between both processes is not fully understood yet, such that even if an identical part is manufactured with EBM, a separate process development still needs to be carried out for LPBF and vice versa. In this study, it was assumed that a similar volume energy density can result in a similar component quality. Therefore, a similar volume energy density was used to assess the component quality in terms of the relative density, mechanical properties, overhang angle, and geometric compliance.

2. Materials and Methods

2.1. Machines

One commercial LPBF and one commercial EBM machine were chosen for this study. The machine characteristics are summarized in Table 1. The LPBF system was equipped with an ytterbium fiber laser with a wavelength of 1070 nm and a maximum power of 400 W. The processed material was shielded from oxidation by an argon atmosphere. If desired, the bottom of the build plate can be heated up to 200 °C [33].

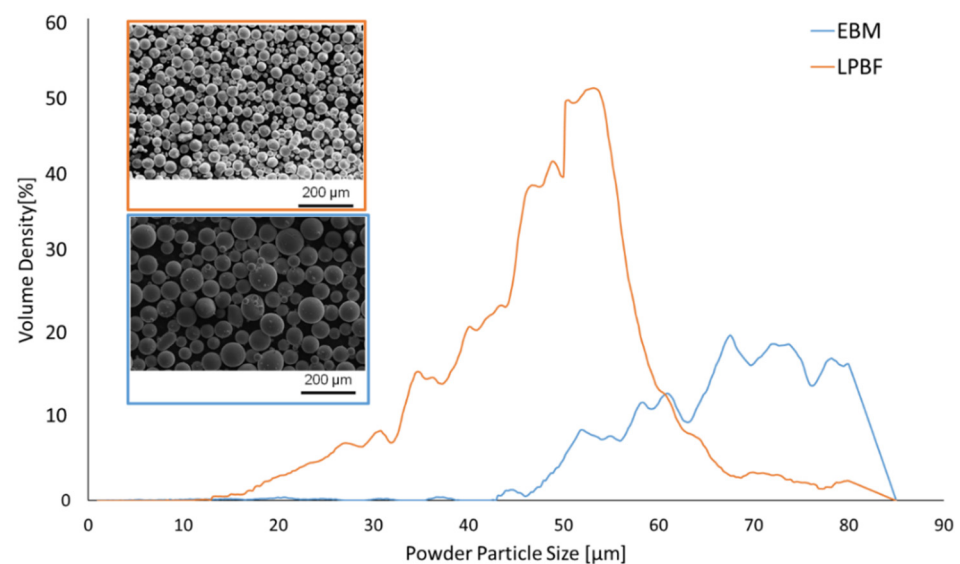
The EBM system was equipped with a lanthanum hexaboride single crystalline cathode. The electrons were accelerated to 60 keV and both focused and deflected by electromagnetic lenses. The machine operated under a controlled vacuum with a helium pressure of up to $\times 10^{-3}$ mbar (i.e., 0.1 Pa) [34].

Table 1. Machine characteristics of the LPBF system and the EBM system.

Machine Characteristics	LPBF System	EBM System
Heat Source	Yb fibre-laser	Single crystalline
Build Volume [mm]	L × B × H 250 × 250 × 250	L × B × H 200 × 200 × 180
Max. Beam Power [W]	400	3000
Atmosphere	Argon	Vacuum
Spot Size [μm]	100	140
Max. scan speed [m/s]	7	8000
Max. preheating temperature [°C]	~200	~1100

2.2. Ti6Al4V Powders

The material used was Ti6Al4V. The powder used in the EBM machine was atomized via the Plasma Rotate Electrode Process (PREP), which yields spherical and uniform powder [13]. The powder used in the LPBF machine was produced by inert gas atomization. Both powders used for EBM and LPBF were recycled. A powder analysis was carried out using Retsch Camsizer X2 (Microtrac Retsch GmbH, Germany) to qualitatively analyze the PSD. The results obtained from both powder samples are compared in Figure 1.

**Figure 1.** Powder particle size distribution and scanning electron microscope (SEM) images for LPBF and EBM powder.

A uniform spherical PSD was observed in the EBM powder. The LPBF powder shows a smaller PSD compared to EBM. This difference in PSD size was confirmed with the SEM analysis.

2.3. Experimental Samples

Cubes of $10 \times 10 \times 10 \text{ mm}^3$ were manufactured using both LPBF and EBM. An inclined surface of 2 mm thickness was printed on one side of the cubes to study overhang behavior (see Figure 2). The angle of inclination was varied using 5° steps.

After the LPBF processing, a 3D scan using GOM ATOS (Carl Zeiss GOM Metrology GmbH, Germany) was taken to determine the geometric compliance and the extent of overhang curling and/or distortion.

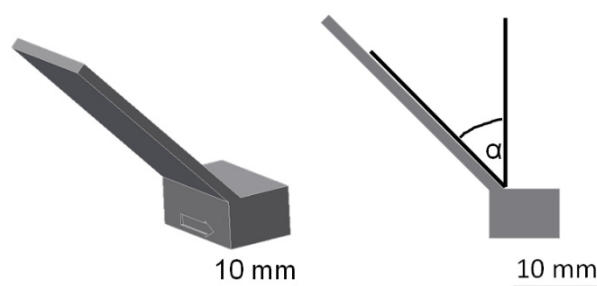


Figure 2. Overhang geometries. The angle α was varied using 5° steps.

2.4. Roughness

The roughness was determined using a Keyence VHX7000 microscope (Keyence Deutschland GmbH, Germany) in build direction away from the inert gas flow on as built and on sand blasted samples. A panorama image of the whole sample was taken at $200\times$ magnification. By analyzing the depth of focus, a 3D model of the surface was obtained.

2.5. Relative Density

Before the relative density measurement, the samples were hot-mounted and ground. The samples were polished by using a polishing wheel and a diamond suspension. The relative density was measured using a Keyence VHX7000 microscope. Using $100\times$ magnification, images of the upper, middle, and lower part of the samples were taken. The built-in Keyence software distinguishes pores and solid material according to changes in the contrast.

2.6. Hardness

The same samples used for the density measurements were also used for hardness measurements. The HV 0.1 hardness was measured with the Qness 30A+ micro-hardness tester (ATM Qness GmbH, Germany). Hardness was measured in the corners and in the middle of every sample. The average values were determined.

2.7. Melt-Pool Dimensions

The mounted samples from the density measurement were etched with hydrofluoric acid for 90 s. Melt-pool depth and width were measured at $300\times$ magnification using a Keyence VHX7000 microscope. Their size was then measured using the built-in Keyence software. An average of 5–7 measurements was calculated.

3. Results and Discussion

3.1. Process Parameters

The process parameters used were provided by the machine suppliers to manufacture dense components. The utilized parameters for the beam power and scan velocity were used to calculate the energy density for the LPBF process (see Table 2). For the EBM system, the beam current was estimated to be 25 mA and the scan speed was estimated to be 6000 mm/s.

Table 2. Utilized process parameters for LPBF and EBM.

Parameter \ Process	LPBF	EBM
Heat Source Power [W]	300 (Laser)	1500 (Electron Beam)
Scan Speed [mm/s]	1000	6000
Hatch Distance [mm]	0.1	0.2
Layer thickness [mm]	0.05	0.05
Volume Energy Density [J/mm^3] *	60	25

* Does not take into consideration absorption.

The energy densities, as shown in Table 2, appear to be very different if it is calculated with the beam power that was set on the machine. An important difference between LPBF and EBM is that in EBM, each powder layer is preheated before melting, maintaining a constant temperature of 700 °C within the build chamber during the process. In contrast, in the LPBF processes, powder is approximately at room temperature before the melting step. In order to compare the volume energy densities more accurately, it is necessary to calculate how much energy per volume is transferred into the powder and how much of it is absorbed. Equation (1) calculates the volume energy density considering the melt-pool size (measured within the course of this study). However, the absorption of each beam by the powder should also be considered. As a result, the volume energy densities change to 10.72 J/mm³ (LPBF) and 8.04 J/mm³ EBM (see Table 3). The volume energy density necessary to heat the powder from room temperature to 700 °C in LPBF is then estimated according to Equation (2). The total volume energy density that melts the powder in LPBF is 9.28 J/mm³. The total volume energy density in the EBM process remains at 8.04 J/mm³. Evidently, independent of the coupling of the energy with the powder layer, the applied energy densities are similar for both processes. This finding shows that the process parameters from the LPBF process can be transferred to the EBM process.

$$E_{V, real} = \frac{P_B}{v_{Scan} * \frac{t}{2} * d} \quad (1)$$

$$E_{V, preheat} = \rho_{powder} * c_p * \Delta T \quad (2)$$

Table 3. Nomenclature and parameters used in calculating volume energy density.

Parameter	LPBF	EBM
Heat Source Power, P_B [W]	300 (Laser)	1500 (Electron Beam)
Scan Speed, v_{scan} [mm/s]	1000	6000
Melt Pool Radius, $t/2$ [mm]	0.07	0.122
Melt Pool Depth, d [mm]	0.16	0.25
Volume Energy Density, E_V (calculated according to Equation (1)) [J/mm ³]	26.79	8.2
Heat Source Absorption [%]	40	98
Volume Energy Density, E_V (calculated according to Equation (1) and considering absorption) [J/mm ³]	10.7	8.04
Ti6Al4V Heat Capacity, c_p [J/g × K]	0.7	-
Powder Bed Density, ρ_{powder} [mg/mm ³]	2.121	-
Temperature difference, ΔT [K]	953.15	-
Real Volume Energy Density, E_V (Equation (1)–Equation (2)) [J/mm ³]	9.28	8.04

3.2. Relative Density

According to literature, both processes are capable of achieving near-fully dense parts with Ti6Al4V [13,35,36]. The achieved densities in this study are illustrated in Figure 3.

The LPBF cubes have an average relative density of 99.98%. These values are in the range of reported density values [37–39]. The spherical pores in the LPBF sample point towards a high energy density, leading to keyholing (see Figure 4). The density of the EBM cubes averages at 99.81%. Increased porosity was observed in the first layers of the EBM specimens (see Figure 4).

A possible reason for the increased pore count on the bottom of the cube could be that small pores expand in size due to the extended time exposed to in situ heat treatment. Körner et al. reported on in situ heat treatment [13]. The use of recycled powder could also play a role due to the reduced flowability of the powder. Within the scope of this study, the relative density in overhangs was also investigated. The results are illustrated in Figure 5.

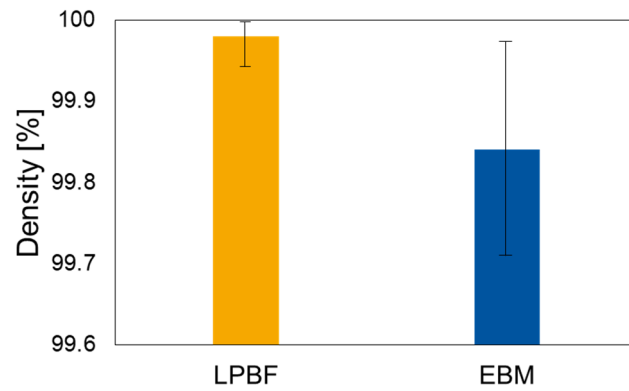


Figure 3. Relative density of LPBF and EBM cubes.

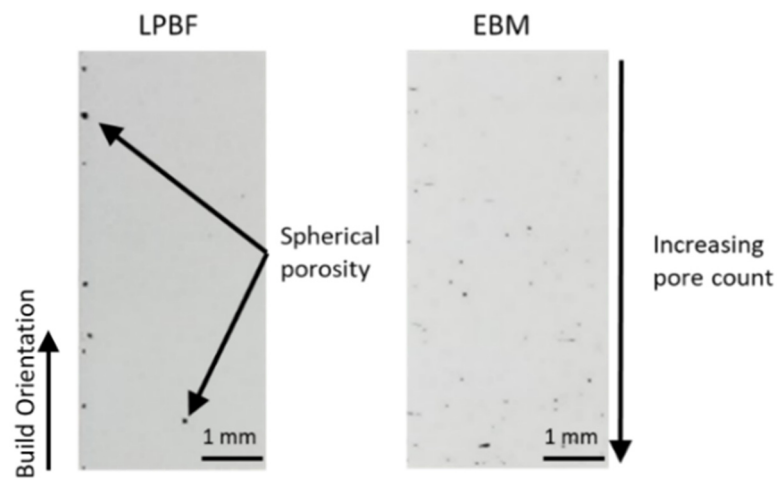


Figure 4. Cross-sections of LPBF and EBM samples.

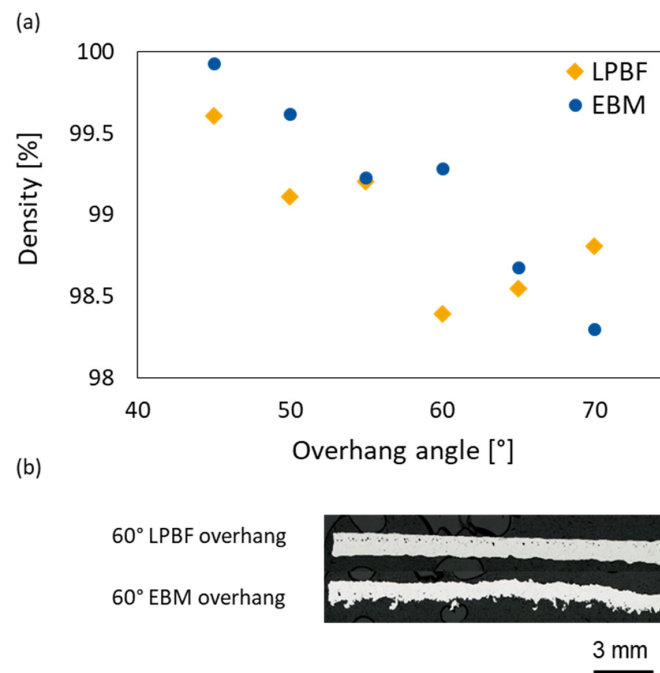


Figure 5. Relative density in LPBF and EBM overhangs. (a) Average overhang density from LPBF and EBM processes plotted against overhang angle. (b) Cross-sections of LPBF and EBM overhangs.

The EBM overhangs are denser compared to those manufactured with LPBF. The density of EBM overhangs decreases linearly with an increasing overhang angle. Pores form mostly on the lower side of the EBM overhang.

The difference in surface roughness can clearly be seen in Figure 5b: The EBM overhang was significantly rougher due to sintering and partially melted particles on the lower side of the overhang. The increase in surface roughness was caused by the preheating/sintering step prior to selective melting.

No significant difference was found regarding the relative density in voluminous LPBF and EBM samples when similar heat inputs (i.e., use of similar volume energy densities) were used. In situ heat treatment showed an effect in EBM overhangs.

3.3. Melt-Pool Size

The melt-pool sizes are shown in Figure 6. The spot sizes of the respective heat sources are listed in Table 1.

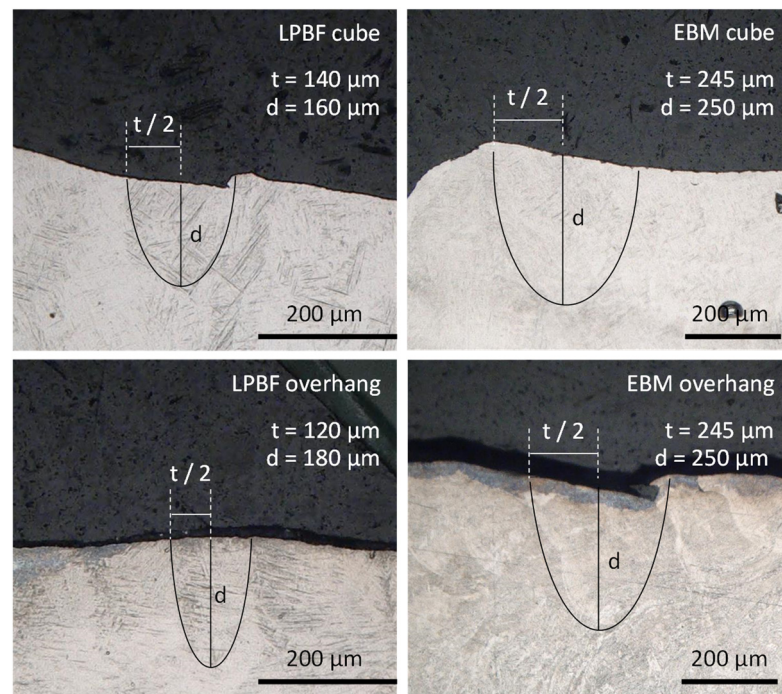


Figure 6. Melt-pool shape and sizes of LPBF and EBM samples.

In the case of LPBF cubes, the melt-pool depth d was approximately $160\ \mu\text{m}$. Its width t was approximately $140\ \mu\text{m}$. A deeper and narrower melt-pool can be observed when overhanging structures are considered. A depth of $180\ \mu\text{m}$ and a width of $120\ \mu\text{m}$ were measured for the LPBF overhanging samples. This difference in shape and size is due to the overheating of the part. Since the overhanging part of the sample was close to the powder with low thermal conductivity, heat piled up in this area. The deep welding effect occurred, which is characterized by a narrow and deeper melt-pool. In general, the melt pools in the EBM components were larger than in LPBF. This can be explained by the preheating strategy in EBM. A constant high temperature was maintained during the build, causing an increase in melt-pool size.

Significant differences in the melt-pool size could be found, although similar volume energy densities were used. Even though absorption was considered in the calculation of the volume energy density, the preheating strategy during EBM significantly affected the melt-pool size.

3.4. Geometrical Accuracy of Overhangs

Figure 7a shows the distortion of EBM overhangs. It can be seen that the distortion increases with an increasing overhang angle, reaching a maximum at a 90° overhang. GOM scans of LPBF samples are similar to EBM results up to 55° overhang, as shown in Figure 7b; however, samples with an overhang angle larger than 65° had to be discontinued during the build due to warping. Based on the available literature on overhangs, the results are as expected [40–43].

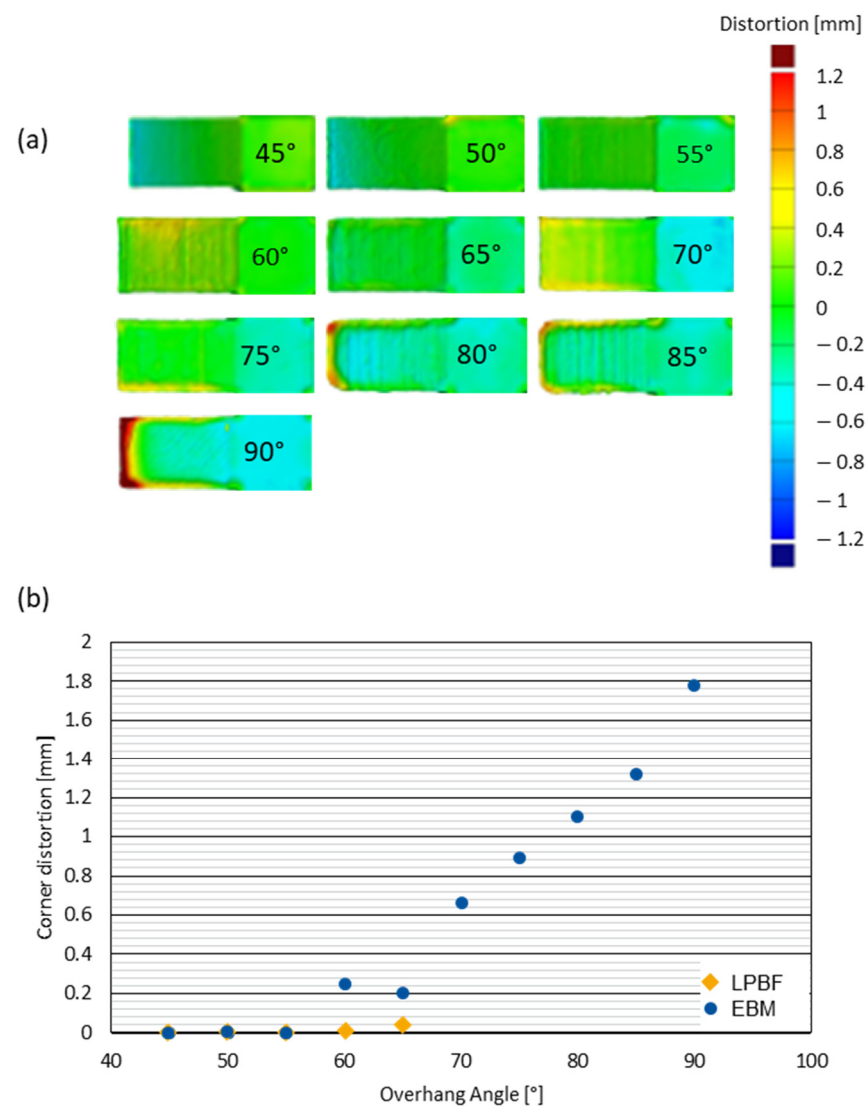


Figure 7. Distortion in overhangs depending on the overhang angle. (a) Visual representation of EBM overhang distortion. (b) EBM and LPBF distortion plotted against overhang angle.

A relationship between the layer thickness, angle, and overhang length was developed by Wang et al. [43]. When increasing the overhang thickness and reducing the overhang angle, the overhang length can be increased and vice versa.

The overhang quality with a reliably buildable overhang angle depends on the energy input due to the differing heat dissipation capacity of solid-supported zones compared to that of powder-supported zones. The heat dissipation capacity in powder-supported zones can be more than 100 times smaller [44]. As can be seen in the results of this study, the distortion increases with an increasing overhang angle for the chosen overhang length. Larger overhang angles (i.e., 90°) can be manufactured with EBM, which was not possible with LPBF in this study.

3.5. Roughness

The as built surfaces obtained from LPBF and EBM are illustrated in Figure 8.

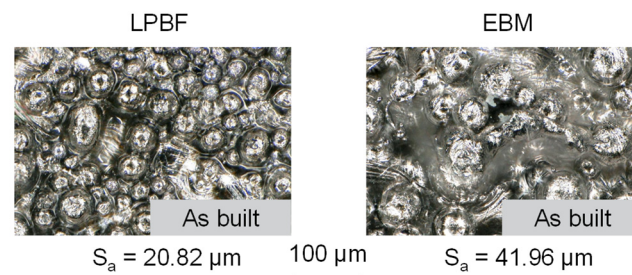


Figure 8. Images of as built LPBF and EBM surfaces.

Partially molten particles are clearly visible on both sample surfaces (i.e., EBM and LPBF). The partial melting of particles to the surface increases the surface roughness. Since larger particles were utilized in EBM (see Figure 1), their impact on the surface roughness was higher than the smaller LPBF particles. The EBM S_a value is twice as large as that of LPBF. This result is in accordance with the results reported in literature [12,13,24,45]. Sand blasted LPBF and EBM surfaces are illustrated in Figure 9.

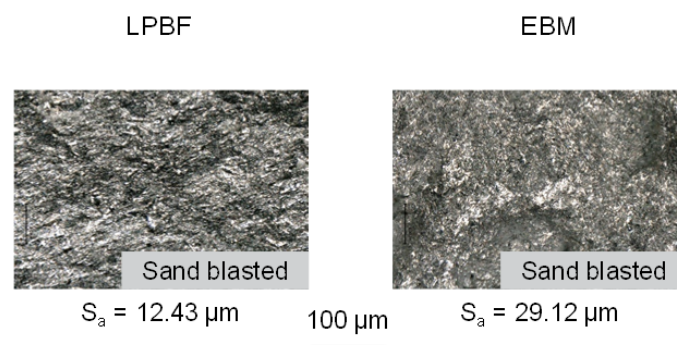


Figure 9. Images of sand blasted LPBF and EBM surfaces.

Sand blasting successfully removes partially molten powder particles. The surface roughness was reduced to 12.43 μm and 29.12 μm for LPBF and EBM, respectively. For the same duration of sand blasting, the roughness of the EBM parts remained higher than that of LPBF parts.

Figure 10a shows the LPBF and EBM overhang surface. As expected, the EBM roughness values surpass those of LPBF by a factor of 2.5. Figure 10b shows a plot of the surface roughness plotted against the overhang angle. Similar R_a values for LPBF were found by Grünewald et al. using a pulsed laser [46].

The results of the surface roughness do not show a direct correlation with the volume energy density. The difference in PSD seems to cause the significant differences in the surface roughness. Further studies on using finer PSD in EBM should be considered while avoiding process instabilities, as reported in the review by Körner et al. [13].

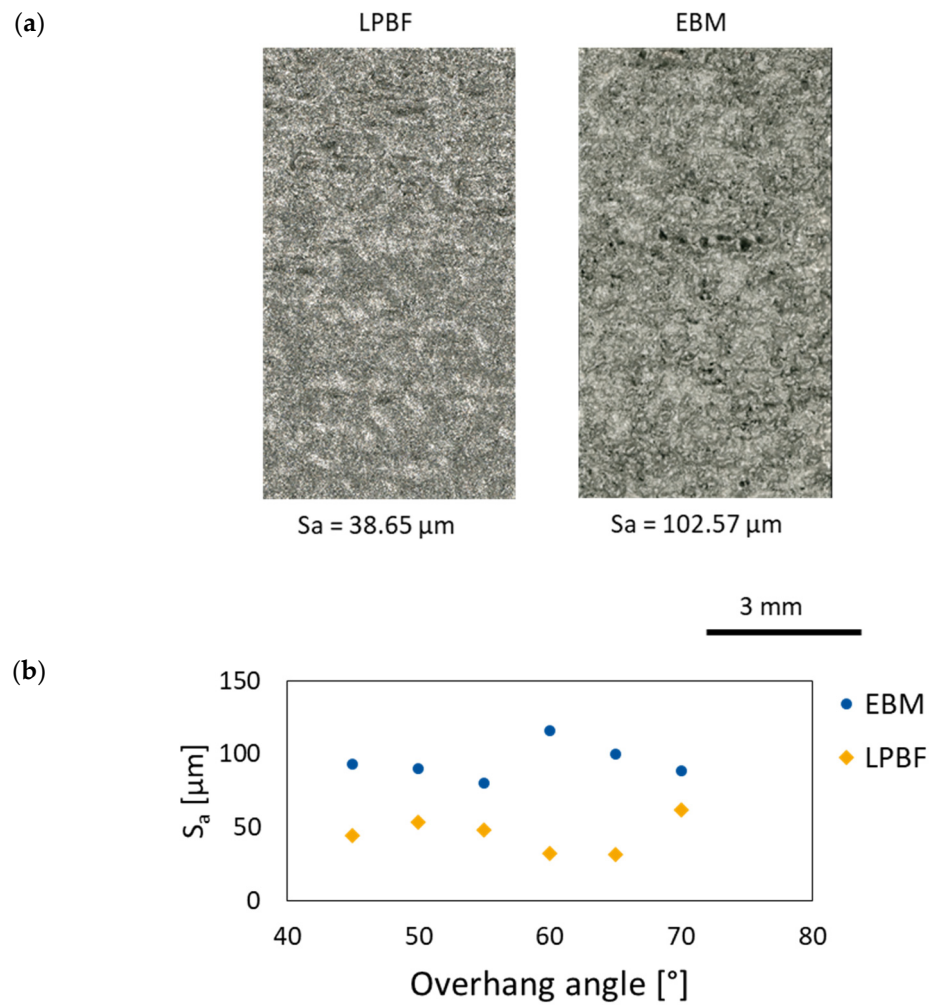


Figure 10. Surface roughness results of LPBF and EBM overhangs. (a) Microscope image of sand blasted LPBF and EBM overhangs. (b) Surface roughness plotted against overhang angle for LPBF and EBM.

3.6. Hardness

The hardness of the LPBF and EBM cubes are compared in Figure 11. The hardness values are in accordance to the results found in literature [47,48]. The hardness values for the overhangs are shown in Figure 12. As can be seen, the LPBF overhangs were at least twice as hard as the EBM overhangs.

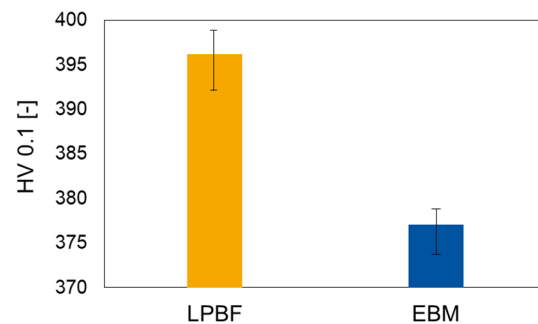


Figure 11. Hardness of LPBF and EBM cubes.

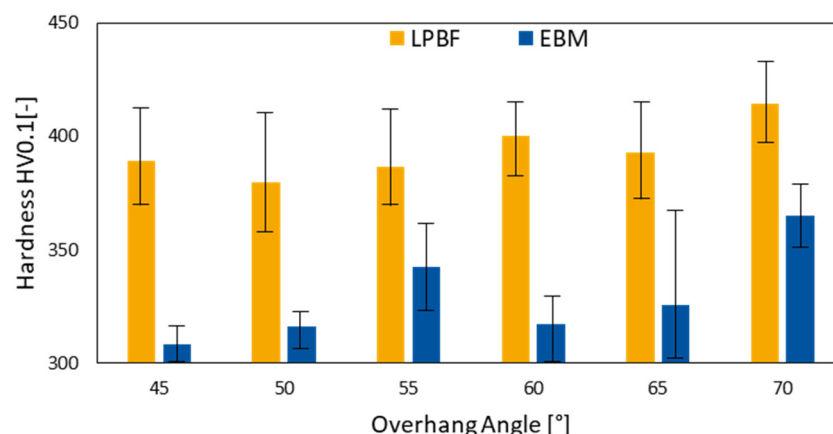


Figure 12. Hardness of LPBF and EBM overhangs.

The reason for the large difference in hardness can be found within the microstructure. The LPBF samples experienced a rapid solidification (10^6 K/s [14]), leading to fine grains that increase the strength according to the Hall-Petch relation [15]. Due to this rapid solidification, the meta-stable strengthening phase martensite forms, as confirmed by Zhao et al. [16]. The solidification rate during EBM was slower (i.e., $\sim 10^3$ – 10^5 K/s [48]) compared to LPBF. The process chamber was held at an elevated temperature (approximately 700 °C), leading to an in situ heat treatment, and cooled down slowly after the build was finished [13]. Consequently, grains were larger and less or no martensite formed. Cao et al. reported that LPBF samples show martensite in as-built conditions, whereas in the heat-treated condition, martensite can decompose [49]. Since an in situ heat treatment occurs during EBM, martensite will decompose, leading to a reduced hardness.

4. Conclusions and Outlook

In this study, the volume energy density for EBM and LPBF was calculated considering absorption. Although a similar volume energy density was used, significant differences in the component quality were observed. The following conclusions can be drawn from this study:

- It has been found that the volume energy density is similar for both LPBF and EBM when absorption is considered.
- While the relative density showed no significant difference, similar results for the surface roughness, melt-pool dimensions, and hardness could not be achieved in LPBF and EBM when manufactured with a similar volume energy density.
- The energy density is not sufficient to guarantee a similar component quality.
- The main reasoning is assumed to be the significant difference in the preheating strategy in LPBF and EBM.
- Similar preheating strategies in LPBF, such as the use of VCSELs [50], are required to achieve a similar component quality in EBM and LPBF.
- The volume energy density and different preheating strategies should be investigated in future studies to understand the possibility of process transferability.

Author Contributions: Conceptualization, S.M.; formal analysis, S.M. and V.A.; methodology, S.M. and V.A.; supervision, J.H.S.; visualization, S.M. and V.A.; writing—original draft preparation, S.M. and V.A.; writing—review and editing, S.M. and J.H.S. All authors have read and agreed to the published version of the manuscript.

Funding: This research received no external funding.

Institutional Review Board Statement: Not applicable.

Informed Consent Statement: Not applicable.

Data Availability Statement: Data is not available.

Conflicts of Interest: The authors declare no conflict of interest.

References

1. Grasso, M.; Colosimo, B.M. Process defects and in situ monitoring methods in metal powder bed fusion: A review. *Surf. Topogr. Metrol. Prop.* **2017**, *28*, 44005. [[CrossRef](#)]
2. Tosi, R.; Leung, C.L.A.; Tan, X.; Muzangaza, E.; Attallah, M.M. Revealing the microstructural evolution of electron beam powder bed fusion and hot isostatic pressing Ti-6Al-4V in-situ shelling samples using X-ray computed tomography. *Addit. Manuf.* **2022**, *57*, 102962. [[CrossRef](#)]
3. Fox, J.C.; Moylan, S.P.; Lane, B.M. Effect of Process Parameters on the Surface Roughness of Overhanging Structures in Laser Powder Bed Fusion Additive Manufacturing. *Procedia CIRP* **2016**, *45*, 131–134. [[CrossRef](#)]
4. Frazier, W.E. Metal Additive Manufacturing: A Review. *J. Mater. Eng. Perform.* **2014**, *23*, 1917–1928. [[CrossRef](#)]
5. Caprio, L.; Chiari, G.; Demir, A.G.; Previtali, B. Development of Novel High Temperature Laser Powder Bed Fusion System for the Processing of Crack-Susceptible Alloys. In Proceedings of the the 29th Annual International Solid Freeform Fabrication (SFF) Symposium—An Additive Manufacturing Conference, Austin, TX, USA, 13–15 August 2018; pp. 2275–2285.
6. Reijonen, J.; Revuelta, A.; Riipinen, T.; Ruusuvoori, K.; Puukko, P. On the effect of shielding gas flow on porosity and melt pool geometry in laser powder bed fusion additive manufacturing. *Addit. Manuf.* **2020**, *32*, 101030. [[CrossRef](#)]
7. Agius, D.; Kourousis, K.; Wallbrink, C. A Review of the As-Built SLM Ti-6Al-4V Mechanical Properties towards Achieving Fatigue Resistant Designs. *Metals* **2018**, *8*, 75. [[CrossRef](#)]
8. Allmen, M.v.; Blatter, A. *Laser-Beam Interactions with Materials*; Springer: Berlin, Heidelberg, 1995; ISBN 978-3-540-59401-7.
9. Fischer, P.; Romano, V.; Weber, H.P.; Karapatis, N.P.; Boillat, E.; Glandon, R. Sintering of commercially pure titanium powder with a Nd:YAG laser source. *Acta Mater.* **2003**, *51*, 1651–1662. [[CrossRef](#)]
10. Tang, H.P.; Qian, M.; Liu, N.; Zhang, X.Z.; Yang, G.Y.; Wang, J. Effect of Powder Reuse Times on Additive Manufacturing of Ti-6Al-4V by Selective Electron Beam Melting. *JOM* **2015**, *67*, 555–563. [[CrossRef](#)]
11. Gibson, I.; Rosen, D.; Stucker, B. *Additive Manufacturing Technologies: 3D Printing, Rapid Prototyping, and Direct Digital Manufacturing*; Springer: New York, NY, USA, 2015.
12. Edwards, P.; Ramulu, M. Fatigue performance evaluation of selective laser melted Ti-6Al-4V. *Mater. Sci. Eng. A* **2014**, *598*, 327–337. [[CrossRef](#)]
13. Körner, C. Additive manufacturing of metallic components by selective electron beam melting—A review. *Int. Mater. Rev.* **2016**, *61*, 361–377. [[CrossRef](#)]
14. Scipioni Bertoli, U.; Guss, G.; Wu, S.; Matthews, M.J.; Schoenung, J.M. In-situ characterization of laser-powder interaction and cooling rates through high-speed imaging of powder bed fusion additive manufacturing. *Mater. Des.* **2017**, *135*, 385–396. [[CrossRef](#)]
15. Porter, D.A.; Easterling, K.E.; Sherif, M. *Phase Transformations in Metals and Alloys*, 3rd ed.; Revised Reprint; CRC Press: Hoboken, NJ, USA, 2009; ISBN 9781439883570.
16. Zhao, X.; Li, S.; Zhang, M.; Liu, Y.; Sercombe, T.B.; Wang, S.; Hao, Y.; Yang, R.; Murr, L.E. Comparison of the microstructures and mechanical properties of Ti-6Al-4V fabricated by selective laser melting and electron beam melting. *Mater. Des.* **2016**, *95*, 21–31. [[CrossRef](#)]
17. Liu, S.; Shin, Y.C. Additive manufacturing of Ti6Al4V alloy: A review. *Mater. Des.* **2019**, *164*, 107552. [[CrossRef](#)]
18. Lewandowski, J.; Mohsen, S. Metal Additive Manufacturing: A Review of Mechanical Properties. *Mater. Res.* **2016**, 151–186. [[CrossRef](#)]
19. Ataee, A.; Li, Y.; Song, G.; Wen, C. *Metal scaffolds processed by electron beam melting for biomedical applications. Metallic Foam Bone*; Elsevier: Amsterdam, The Netherlands, 2017; pp. 83–110. ISBN 9780081012895.
20. Tan, X.; Kok, Y.; Tor, S.B.; Chua, C.K. Application of Electron Beam Melting (EBM) in Additive Manufacturing of an Impeller. In Proceedings of the 1st International Conference on Progress in Additive Manufacturing (Pro-AM 2014), Singapore, 26–28 May 2014; pp. 327–332.
21. Béraud, N.; Vignat, F.; Villeneuve, F.; Dendievel, R. Improving dimensional accuracy in EBM using beam characterization and trajectory optimization. *Addit. Manuf.* **2017**, *14*, 1–6. [[CrossRef](#)]
22. Karlsson, J.; Snis, A.; Engqvist, H.; Lausmaa, J. Characterization and comparison of materials produced by Electron Beam Melting (EBM) of two different Ti-6Al-4V powder fractions. *J. Mater. Processing Technol.* **2013**, *213*, 2109–2118. [[CrossRef](#)]
23. Petrovic, V.; Niñerola, R. Powder recyclability in electron beam melting for aeronautical use. *Aircr. Eng. Aerosp. Tech.* **2015**, *87*, 147–155. [[CrossRef](#)]
24. Klingvall Ek, R.; Rännar, L.-E.; Bäckstöm, M.; Carlsson, P. The effect of EBM process parameters upon surface roughness. *RPJ* **2016**, *22*, 495–503. [[CrossRef](#)]
25. Galati, M.; Minetola, P.; Rizza, G. Surface Roughness Characterisation and Analysis of the Electron Beam Melting (EBM) Process. *Materials* **2019**, *12*, 2211. [[CrossRef](#)] [[PubMed](#)]
26. Al-Bermani, S.S.; Blackmore, M.L.; Zhang, W.; Todd, I. The Origin of Microstructural Diversity, Texture, and Mechanical Properties in Electron Beam Melted Ti-6Al-4V. *Met. Mat. Trans. A* **2010**, *41*, 3422–3434. [[CrossRef](#)]
27. Koike, M.; Martinez, K.; Guo, L.; Chahine, G.; Kovacevic, R.; Okabe, T. Evaluation of titanium alloy fabricated using electron beam melting system for dental applications. *J. Mater. Processing Technol.* **2011**, *211*, 1400–1408. [[CrossRef](#)]

28. Antonysamy, A. Microstructure, Texture and Mechanical Property Evolution during Additive Manufacturing of Ti6Al4V Alloy for Aerospace Applications. Ph.D. Thesis, University of Manchester, Manchester, UK, 2012.
29. Harun, W.S.W.; Manam, N.S.; Kamariah, M.S.I.N.; Sharif, S.; Zulkifly, A.H.; Ahmad, I.; Miura, H. A review of powdered additive manufacturing techniques for Ti-6Al-4V biomedical applications. *Powder Technol.* **2018**, *331*, 74–97. [[CrossRef](#)]
30. Qian, M.; Xu, W.; Brandt, M.; Tang, H.P. Additive manufacturing and postprocessing of Ti-6Al-4V for superior mechanical properties. *MRS Bull.* **2016**, *41*, 775–784. [[CrossRef](#)]
31. Fousová, M.; Vojtěch, D.; Doubrava, K.; Daniel, M.; Lin, C.-F. Influence of Inherent Surface and Internal Defects on Mechanical Properties of Additively Manufactured Ti6Al4V Alloy: Comparison between Selective Laser Melting and Electron Beam Melting. *Materials* **2018**, *11*, 537. [[CrossRef](#)] [[PubMed](#)]
32. Murr, L.E.; Gaytan, S.M.; Ramirez, D.A.; Martinez, E.; Hernandez, J.; Amato, K.N.; Shindo, P.W.; Medina, F.R.; Wicker, R.B. Metal Fabrication by Additive Manufacturing Using Laser and Electron Beam Melting Technologies. *J. Mater. Sci. Technol.* **2012**, *28*, 1–14. [[CrossRef](#)]
33. EOS GmbH. LPBF System EOS M290. Available online: <https://docplayer.org/1881544-Technische-beschreibung-eos-m-290-technische-beschreibung-1-eos-m-290-stand-april-2014.html> (accessed on 9 July 2022).
34. GE Additive. Arcam EBM Q10plus. Available online: https://www.ge.com/additive/sites/default/files/2020-04/EBM_Q10plus_Bro_4_US_EN_v1_0.pdf (accessed on 9 July 2022).
35. Sing, S.L.; An, J.; Yeong, W.Y.; Wiria, F.E. Laser and electron-beam powder-bed additive manufacturing of metallic implants: A review on processes, materials and designs. *J. Orthop. Res.* **2016**, *34*, 369–385. [[CrossRef](#)] [[PubMed](#)]
36. Pobel, C.R.; Osmanlic, F.; Lodes, M.A.; Wachter, S.; Körner, C. Processing windows for Ti-6Al-4V fabricated by selective electron beam melting with improved beam focus and different scan line spacings. *RPJ* **2019**, *25*, 665–671. [[CrossRef](#)]
37. Yadroitsev, I.; Krakhmalev, P.; Yadroitsava, I.; Du Plessis, A. Qualification of Ti6Al4V ELI Alloy Produced by Laser Powder Bed Fusion for Biomedical Applications. *JOM* **2018**, *70*, 372–377. [[CrossRef](#)]
38. Yasa, E.; Deckers, J.; Kruth, J.-P. The investigation of the influence of laser re-melting on density, surface quality and microstructure of selective laser melting parts. *RPJ* **2011**, *17*, 312–327. [[CrossRef](#)]
39. Vandenbroucke, B.; Kruth, J.-P. Selective laser melting of biocompatible metals for rapid manufacturing of medical parts. *RPJ* **2007**, *13*, 196–203. [[CrossRef](#)]
40. Wang, D.; Yang, Y.; Zhang, M.; Lu, J.; Liu, R.; Xiao, D. Study on SLM fabrication of precision metal parts with overhanging structures. In Proceedings of the 2013 IEEE International Symposium on Assembly and Manufacturing (ISAM), Xi'an, China, 30 July–2 August 2013; pp. 222–225.
41. Gruber, S.; Grunert, C.; Riede, M.; López, E.; Marquardt, A.; Brueckner, F.; Leyens, C. Comparison of dimensional accuracy and tolerances of powder bed based and nozzle based additive manufacturing processes. *J. Laser Appl.* **2020**, *32*, 32016. [[CrossRef](#)]
42. Thomas, D. The Development of Design Rules for Selective Laser Melting. Ph.D Thesis, University of Wales, National Centre for Product Design & Development Research, Cardiff, UK, 2009.
43. Di, W.; Yang, Y.; Yi, Z.; Su, X. Research on the fabricating quality optimization of the overhanging surface in SLM process. *Int. J. Adv. Manuf. Technol.* **2013**, *65*, 1471–1484. [[CrossRef](#)]
44. Kruth, J.-P.; Bartolo, P.J. Feedback control of selective laser melting. In Proceedings of the 3rd International Conference on Advanced Research in Virtual and Rapid Prototyping, Leiria, Portugal, 24–29 September 2007; pp. 521–527.
45. Chen, Z.; Wu, X.; Tomus, D.; Davies, C.H.J. Surface roughness of Selective Laser Melted Ti-6Al-4V alloy components. *Addit. Manuf.* **2018**, *21*, 91–103. [[CrossRef](#)]
46. Grünwald, J.; Clarkson, P.; Salvesson, R.; Fey, G.; Wudy, K. Influence of Pulsed Exposure Strategies on Overhang Structures in Powder Bed Fusion of Ti6Al4V Using Laser Beam. *Metals* **2021**, *11*, 1125. [[CrossRef](#)]
47. Yadroitsev, I.; Krakhmalev, P.; Yadroitsava, I. Titanium Alloys Manufactured by In Situ Alloying During Laser Powder Bed Fusion. *JOM* **2017**, *69*, 2725–2730. [[CrossRef](#)]
48. Hrabec, N.; Quinn, T. Effects of processing on microstructure and mechanical properties of a titanium alloy (Ti-6Al-4V) fabricated using electron beam melting (EBM), Part 2: Energy input, orientation, and location. *Mater. Sci. Eng. A* **2013**, *573*, 271–277. [[CrossRef](#)]
49. Cao, S.; Zou, Y.; Voon Samuel Lim, C.; Wu, X.; Cao, S.; Zou, Y.; Wu, X. Review of laser powder bed fusion (LPBF) fabricated Ti-6Al-4V: Process, post-process treatment, microstructure, and property. *Light Adv. Manuf.* **2021**, *2*, 313–332. [[CrossRef](#)]
50. Vogelpoth, A. VCSEL Preheating for Laser Powder Bed Fusion. Available online: https://webcache.googleusercontent.com/search?q=cache:XUbsnUliUXkJ:https://www.ilt.fraunhofer.de/content/dam/ilt/en/documents/annual_reports/AR18/TF2/AR18_P54_VCSEL_preheating_for_laser_powder_bed_fusion.pdf+&cd=4&hl=de&ct=clnk&gl=de&client=firefox-b-d (accessed on 28 July 2022).